ATLAS CONF Note

ATLAS-CONF-2018-019

31st May 2018

Search for exotic decays of the Higgs boson to at least one photon and missing transverse momentum using 79.8 fb^{-1} of proton–proton collisions collected at $\sqrt{s}$ = 13 TeV with the ATLAS detector

The ATLAS Collaboration

A search for Standard Model Higgs bosons decaying into at least one photon and missing transverse momentum is performed using 79.8 fb^{-1} of proton–proton collisions collected at $\sqrt{s}$ = 13 TeV with the ATLAS detector. The photon can arise from a Higgs boson decaying into one or two neutralinos, which in turn decay into a gravitino and photon. Higgs bosons produced in association with a Z boson are considered in order to reduce the number of background events. No excess with respect to the Standard Model prediction is observed. Assuming a Standard Model Zh production cross-section, the branching fraction of a Higgs boson to neutralinos or neutralino/gravitino is constrained to be less than 5–11% at the 95% confidence level for nearly massless gravitinos.

ATLAS-CONF-2018-019
04 June 2018

1 Introduction

In 2012, the discovery of a particle consistent with the Higgs boson (h) was announced by the ATLAS [1] and CMS [2] collaborations. Since then, measurements of its properties and couplings to Standard Model (SM) fermions and gauge bosons have been a cornerstone of the Large Hadron Collider (LHC) [3] research program. No significant deviations from SM predictions have been observed in combined measurements from ATLAS and CMS, and along with minimal assumptions, the branching fraction (BF) of the Higgs boson to new processes beyond the Standard Model (BSM) is constrained to be less than 34% at the 95% confidence level [4, 5].

A wide variety of theories predict decays of the Higgs boson to BSM particles [6]. Supersymmetry (SUSY) [7–12] is an interesting extension of the SM that includes additional particles that differ from their SM partners by half a unit of spin. In particular, SUSY could address the hierarchy problem and other issues in modern particle physics. In a class of SUSY models called Gauge Mediated Supersymmetry Breaking (GMSB) [13–17], there are some mechanisms that produce a 125 GeV Higgs boson consistent with current measurements [18–22]. In GMSB models, the Higgs boson can decay to a very light gravitino $\tilde{G}$ (the lightest supersymmetric particle, LSP) and a neutralino $\tilde{\chi}_1^0$ (the next-to-lightest supersymmetric particle, NLSP) [23]. A diagram of this process is shown in Figure 1(a). The neutralino in turn decays to a photon (γ) and a gravitino, leading to a photon and missing transverse momentum in the final state. This process can also be realized in the context of Next-to-Minimal Supersymmetric Standard Models (nMSSM) [24, 25], where the Higgs boson decays to a singlino $\tilde{\chi}_1^0$ (LSP) and bino $\tilde{\chi}_2^0$ (NSLP) which in turn decays to a photon and $\tilde{\chi}_1^0$. In nMSSM scenarios the LSP mass is less constrained than in GMSB models where the gravitino is nearly massless.

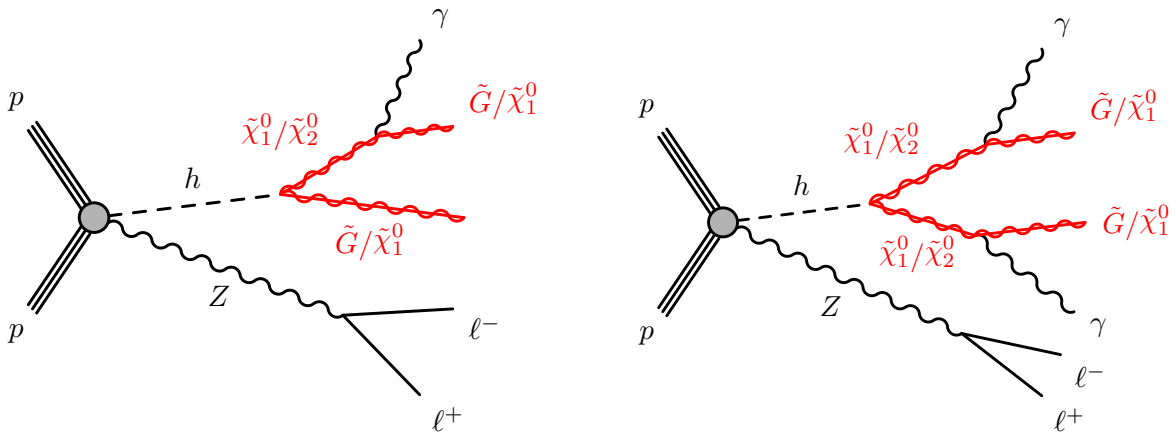

(a) $h \to \tilde{\chi}_1^0\tilde{G} \to \gamma\tilde{G}\tilde{G}$ / $h \to \tilde{\chi}_2^0\tilde{\chi}_1^0 \to \gamma\tilde{\chi}_1^0\tilde{\chi}_1^0$

(b) $h \to \tilde{\chi}_1^0\tilde{\chi}_1^0 \to \gamma\tilde{G}\gamma\tilde{G}$ / $h \to \tilde{\chi}_2^0\tilde{\chi}_2^0 \to \gamma\tilde{\chi}_1^0\gamma\tilde{\chi}_1^0$

Figure 1: Diagrams for the production, in association with a Z, and GMSB/nMSSM decay of the Higgs boson leading to a final state of two leptons + (a) $\gamma + E_{\mathrm{T}}^{\mathrm{miss}}$ and (b) $\gamma\gamma + E_{\mathrm{T}}^{\mathrm{miss}}$. The $\gamma + E_{\mathrm{T}}^{\mathrm{miss}}$ final state is produced when $m_h/2 < m_{\tilde{\chi}_1^0}(m_{\tilde{\chi}_2^0}) < m_h$, while the $\gamma\gamma + E_{\mathrm{T}}^{\mathrm{miss}}$ final state is realized when $m_{\tilde{\chi}_1^0}(m_{\tilde{\chi}_2^0}) < m_h/2$.

In GMSB (nMSSM) models, the Higgs boson can decay to an $\tilde{\chi}_1^0$ ($\tilde{\chi}_2^0$) and $\tilde{G}$ ($\tilde{\chi}_2^0$) in the case when $m_h/2 < m_{\tilde{\chi}_1^0}(m_{\tilde{\chi}_2^0}) < m_h$ as this is the only kinematically allowed decay. Alternatively, when $m_{\tilde{\chi}_1^0}(m_{\tilde{\chi}_2^0}) < m_h/2$, the Higgs boson is allowed to decay directly to two NLSP neutralinos (bino-like neutralinos), each

decaying to a photon and LSP gravitino (singlino-like neutralino) [26]. A diagram of this process can be seen in Figure 1(b). This scenario is expected to dominate when $m_{\tilde{\chi}_1^0}(m_{\tilde{\chi}_2^0}) < m_h/2$.

Higgs bosons produced in association with a Z boson decaying to muons or electrons are considered in order to reduce backgrounds and provide clean kinematic handles on the Higgs boson decay products. This note presents a search using events containing two same flavor opposite-sign, isolated electrons or muons, at least one isolated photon and missing transverse momentum. The search is performed using 79.8 fb^{-1} of proton–proton (pp) collisions collected at $\sqrt{s} = 13$ TeV with the ATLAS detector at the LHC in 2015, 2016, and 2017. No significant excess over the SM prediction is found, and the total number of expected and observed events in the signal region (see Section 3) is used to set limits on $(\sigma/\sigma_{SM}) \times$ BF. Here, σ refers to the cross-section of a Higgs boson produced in association with a Z from pp collisions at $\sqrt{s} = 13$ TeV, and BF is the branching fraction of the Higgs boson to a $\gamma + E_{\mathrm{T}}^{\mathrm{miss}}$ or $\gamma\gamma + E_{\mathrm{T}}^{\mathrm{miss}}$ final state.

The ATLAS experiment sought these processes in Run 1 by probing the vector boson fusion (VBF) production mode of the Higgs boson [27]. An exclusion of $(\sigma/\sigma_{SM}) \times \mathrm{BF}(h \to \tilde{\chi}_1^0\tilde{\chi}_1^0 \to \gamma\tilde{G}\gamma\tilde{G})$ above 20–35% and $(\sigma/\sigma_{SM}) \times \mathrm{BF}(h \to \tilde{\chi}_1^0\tilde{G} \to \gamma\tilde{G}\tilde{G})$ above 25–80% was derived at the 95% confidence level (CL) for the majority of phase space, depending on the masses of the NLSP and LSP. The CMS experiment sought a similar signature using the gluon–gluon fusion and ZH production modes, and excluded (σ/σ_{SM}) $\times$ BFs above 7–13% at the 95% CL for models with massless gravitinos [28].

2 Data and Simulated Samples

The ATLAS detector [29] was used to collect pp collisions at $\sqrt{s} = 13$ TeV during the 2015–2017 running periods, resulting in an integrated luminosity of 79.8 fb^{-1}. The data were recorded using a two-level trigger system [30] that requires one or two lepton candidates in the event. In order to keep the data-collection rate stable, different p_{T} thresholds[1] were used during different data-taking periods, which are summarized in Table 1. The average number of pp interactions per bunch crossing, $\langle\mu\rangle$, was 13.4 in 2015, 25.1 in 2016, and 38.8 in 2017.

While the dominant background processes are derived from control regions (see Section 4), the $Z\gamma$, $Z\gamma\gamma$, $W\gamma\gamma$ and $t\bar{t}\gamma$ contributions are modeled with Monte Carlo (MC) simulation. Events in an electron rich control region are also compared with WZ MC simulation. Events containing a vector boson and one (two) photons or electrons are simulated with the Sherpa 2.2.2 [31] event generator. Matrix elements including all diagrams with 3 (4) electroweak couplings are calculated with up to 3 (4) partons at next-to-leading order and merged with the parton shower according to the ME+PS@NLO prescription [32]. The NNPDF3.0 NNLO PDF set [33] is used in conjunction with a dedicated parton shower tuning developed by the Sherpa authors [34]. Events containing a top–antitop quark pair and a photon were generated using MadGraph5_aMC@NLO version 2.3.3 [35] at leading order (LO). Samples were generated with the NNPDF2.3 LO PDF set [36], using the A14 set of tuned parameters [37] of Pythia 8.186 [38–40] for the

[1] ATLAS uses a right-handed coordinate system with its origin at the nominal interaction point (IP) in the center of the detector and the z-axis along the beam pipe. The x-axis points from the IP to the center of the LHC ring, and the y-axis points upwards. Cylindrical coordinates (r, ϕ) are used in the transverse plane, ϕ being the azimuthal angle around the z-axis. The pseudorapidity is defined in terms of the polar angle θ as $\eta = -\ln\tan(\theta/2)$. When dealing with massive jets and particles, the rapidity $y = 1/2\ln(E + p_z)/(E - p_z)$ is used, where E is the jet energy and p_z is the z-component of the jet momentum. Angular distance is measured in units of $\Delta R \equiv \sqrt{(\Delta\eta)^2 + (\Delta\phi)^2}$.

	Single lepton threshold [GeV]	Two lepton thresholds [GeV]
Electron trigger year		
2015	24	12, 12
2016	26	17, 17
2017	26	17, 17 and 24, 24
Muon trigger year		
2015	20	18, 8
2016	26	22, 8
2017	26	22, 8

Table 1: Lepton p_{T} trigger threshold for electrons and muons, collected in the 2015–2017 data taking periods requiring one or two leptons. In a given year, the logical OR of electron and muon triggers, for both one and two objects, is taken.

parton-shower and hadronization simulation. The generated events were passed through a full detector simulation based on GEANT 4 [41, 42].

Signal events for the $Z \to \ell\ell$ and $h \to \tilde{\chi}_1^0\tilde{\chi}_1^0 \to \gamma\tilde{G}\gamma\tilde{G}$ or $h \to \tilde{\chi}_1^0\tilde{G} \to \gamma\tilde{G}\tilde{G}$ processes were produced at LO with MADGRAPH5_aMC@NLO using the SUSY simplified model framework [43, 44]. Samples were generated with the NNPDF2.3 LO PDF set, using the A14 set of tuned parameters of PYTHIA 8.186 for the parton-shower and hadronization simulation. The signal samples are processed through a fast detector simulation based on a parameterisation of the performance of the calorimeters [45]. The cross-section for a SM Higgs boson produced in association with a Z boson is taken from Ref. [46].

Multiple overlaid proton–proton collisions are simulated with the soft QCD processes of PYTHIA 8.186 using the A2 set of tuned parameters [47] and the MSTW2008LO PDF set. The simulated events are weighted to reproduce the distribution of average number of interactions per bunch crossing observed in data.

3 Event Selection

This section describes the object and event selections used for this analysis. While objects are selected using the baseline criteria described in Section 3.1, more stringent requirements are made for the signal region (see Section 3.2), control regions, and validation regions (see Section 4).

3.1 Object Selection

Electrons and photons are reconstructed from clusters of energy deposited in the electromagnetic calorimeter [48]. In the case of electrons, a charged particle track must be associated with the a calorimeter cluster. Photons can directly enter the calorimeter while leaving no charged particle track, or convert

into a pair of electrons when interacting with inner detector material resulting in a conversion vertex, in which case tracking information is also used to reconstruct the particle. Electrons (photons) are required to have $|\eta| < 2.47$ (2.37), with transverse momentum p_{T} (transverse energy E_{T}) larger than 10 (20) GeV. Additionally, photons and electrons in the transition region $1.37 < |\eta| < 1.52$ between the barrel and endcap calorimeters are rejected. Electrons are required to pass the *medium* likelihood based identification working point [49], as well as track and calorimeter-based isolation requirements such that the efficiency of the selection is 95% at 25 GeV and 99% at 60 GeV [50, 51]. For photons the calorimeter-based isolation requirement is as follows: after correcting for contributions from pileup and the photon itself, transverse energy deposited in a cone of size $\Delta R = 0.4$ surrounding the energy deposition of the photon, $E_{\mathrm{T}}^{0.4}$, must satisfy the relation $E_{\mathrm{T}}^{0.4} < 2.75\,\mathrm{GeV} + 0.22 E_{\mathrm{T}}$. A track based variable defined as the sum of charged-particle track p_{T} ($p_{\mathrm{T}} > 1$ GeV) within $\Delta R = 0.2$ is required to be less than $0.05 E_{\mathrm{T}}$. Two identification criteria are considered for photons: the so-called *tight* selection provides a pure sample of photons, while *loose* relaxes the criteria in order to provide a jet enriched sample for background studies [50].

Muon candidates are reconstructed from tracks in the inner detector and muon spectrometer, and are required to have $|\eta| < 2.7$ and $p_{\mathrm{T}} > 10\,\mathrm{GeV}$. They are also required to pass the *medium* identification working point [52] based on charged-particle track information, and to pass the same track and calorimeter isolation criteria that are applied to electrons.

Jets are reconstructed from calorimeter clusters using the anti-k_t algorithm with distance parameter $R = 0.4$ [53]. A calibration is applied [54], and additional criteria are required to reject fake jets [55] as well as jets from different pp collisions [56]. Only jets with rapidity $|y| < 4.4$ and $p_{\mathrm{T}} > 20\,\mathrm{GeV}$ are considered.

Potential ambiguities between measured objects are resolved by using an overlap removal procedure. First, jets are removed if they are within $\Delta R = 0.2$ of an electron, and electrons are removed if they are within $\Delta R = 0.4$ of any remaining jets. Muons are removed if they are within $\Delta R = 0.4$ of a jet, except if the jet has fewer than three charged-particle tracks associated with it, in which case the jet is removed instead. The rate of photons faking leptons is reduced by removing photons within $\Delta R = 0.4$ of an electron or muon. Finally, jets are removed if they are within $\Delta R = 0.4$ of a photon.

Missing transverse momentum ($E_{\mathrm{T}}^{\mathrm{miss}}$) is defined as the magnitude of the negative vector sum of the transverse momentum of the remaining electrons, muons, photons and jets. An additional term accounting for energy not associated with a measured object is included by considering the remaining charged-particle tracks associated with the hard-scatter vertex in the event [57].

3.2 Event Selection

Signal events are characterized by moderate $E_{\mathrm{T}}^{\mathrm{miss}}$, and the $Z \to \ell\ell$ pair balancing the $h \to \gamma E_{\mathrm{T}}^{\mathrm{miss}}$ system in the transverse plane. Only *tight*, isolated photons with $p_{\mathrm{T}} > 25\,\mathrm{GeV}$ are considered, and the vector sum of the two highest-p_{T} photons (or one if two are not available) with the $E_{\mathrm{T}}^{\mathrm{miss}}$ defines the $\gamma E_{\mathrm{T}}^{\mathrm{miss}}$ system.

The Z boson system is composed of two opposite-sign electrons or muons, where the highest (second highest) p_{T} lepton must have $p_{\mathrm{T}} > 25$ (20) GeV. The dilepton invariant mass must be within 10 GeV of the Z boson mass, and the separation of the leptons in ϕ must be less than 1.4 rad. To reduce contamination from diboson processes the event must have exactly 2 leptons.

Background rejection is achieved predominately by selecting events with $E_{\mathrm{T}}^{\mathrm{miss}} > 95\,\mathrm{GeV}$. To improve the resolution of the $E_{\mathrm{T}}^{\mathrm{miss}}$, and to reduce contamination from background processes containing top quarks,

events containing jets with $p_{\mathrm{T}} > 30$ GeV are also rejected. In addition, two variables are defined to exploit the balance of the Z and $\gamma E_{\mathrm{T}}^{\mathrm{miss}}$ systems and reject Z + jet events.

1. $\Delta\phi_{\ell\ell,\gamma E_{\mathrm{T}}^{\mathrm{miss}}}$: the absolute separation in ϕ of the two-lepton system and the $\gamma E_{\mathrm{T}}^{\mathrm{miss}}$ system.

2. $\mathrm{Bal}_{p_{\mathrm{T}}}$: the asymmetry of the $\ell\ell$ and $\gamma E_{\mathrm{T}}^{\mathrm{miss}}$ systems, $\frac{|p_{\mathrm{T}}^{\ell\ell} - p_{\mathrm{T}}^{\gamma E_{\mathrm{T}}^{\mathrm{miss}}}|}{p_{\mathrm{T}}^{\gamma E_{\mathrm{T}}^{\mathrm{miss}}}}$.

A modest improvement in the signal-to-background ratio is achieved by selecting events with $\mathrm{Bal}_{p_{\mathrm{T}}} < 0.2$ and $\Delta\phi_{\ell\ell,\gamma E_{\mathrm{T}}^{\mathrm{miss}}} > 2.8$. The selection described above is designed to optimize the search over the full parameter space.

During the data taking periods considered in the analysis, 140 M events were selected by the lepton triggers shown in Table 1.

4 Background Modelling

There are four background sources which can leave signatures in the detector similar to the signal process. These can be grouped into:

- Backgrounds where an electron is mis-identified as a photon, primarily coming from $WZ \to e\nu\ell\ell$.
- Backgrounds with resonant Z bosons that contain a real photon, coming largely from SM $Z\gamma$.
- Backgrounds generally coming from Z + jets where a jet is mis-identified as a photon.
- Backgrounds with non-resonant leptons, consistent with the Z mass, that contain a real photon.

Section 4.1 discusses the background estimation from electrons faking photons ($e \to \gamma$) using a data-driven method. These fakes predominantly come from $WZ \to e\nu\ell\ell$ events where the electron is mis-identified as a photon. The shape of the background from SM $Z\gamma$ production is estimated using simulated events while the normalization is obtained from a control region with lower $E_{\mathrm{T}}^{\mathrm{miss}}$, as described in Section 4.2. This estimation is then validated in an intermediate $E_{\mathrm{T}}^{\mathrm{miss}}$ region. Section 4.3 expands upon the background estimation of jets faking photons (j $\to \gamma$). These events mostly come from Z+jets events but other processes such as diboson and $t\bar{t}$ production may also contribute. The method to estimate the j $\to \gamma$ background is validated in a region with unbalanced events ($\Delta\phi_{\ell\ell,\gamma E_{\mathrm{T}}^{\mathrm{miss}}} < 2.2$) and uses a higher, asymmetric dilepton mass window $m_{\ell\ell}^{\mathrm{win}}$ to remove the radiative $Z\gamma$ contamination.

Table 2 shows the different regions defined in the analysis. Backgrounds from $t\bar{t}\gamma$ and $V\gamma\gamma$ (non-resonant leptons, real photon) are estimated with MC simulation to be negligible. The number of background events from SM Higgs boson decays ($h \to \gamma\gamma, WW, \tau\tau$) is also negligible. The cross section of $Zh \to \ell\ell Z\gamma \to \ell\ell\nu\nu\gamma$ is 0.018 fb [46, 58] and is therefore neglected. The upper limit on the production cross section for $h \to Z\gamma \to \ell\ell\gamma$ is observed to be 6.6 times the SM prediction [59], making this background negligible as well.

Cut	CR WZ	CR Zγ	VR Zγ	VR jets	SR
Pass triggers and vetos	✓	✓	✓	✓	✓
2 signal leptons	✓	✓	✓	✓	✓
At least 1 signal photon	> 25 GeV(electron)	> 25 GeV	> 25 GeV	> 25 GeV	> 25 GeV
$m_{\ell\ell}^{\text{win}}$	81-101 GeV	81-101 GeV	81-101 GeV	85-120 GeV	81-101 GeV
$E_{\text{T}}^{\text{miss}}$	> 95 GeV	20-35 GeV	35-70 GeV	> 35 GeV	> 95 GeV
$\text{Bal}_{p_{\text{T}}}$	< 0.2	< 0.2	< 0.2	-	< 0.2
$\Delta\phi_{\ell\ell,\gamma E_{\text{T}}^{\text{miss}}}$	> 2.8	-	-	< 2.2	> 2.8
$\Delta\phi(\ell,\ell)$	< 1.4	< 2.0	< 2.0	-	< 1.4

Table 2: Table of selection criteria for the different control, validation, and signal regions used in the analysis. The '(electron)' in the CR WZ signifies the condition of an *medium* electron being required in place of the signal photon.

4.1 Backgrounds with an electron faking a photon, primarily coming from $WZ \to e\nu\ell\ell$

Electrons and photons leave a very similar signature in the calorimeter; the primary distinction between the two is the existence of a track originating from the primary vertex for an electron. A small fraction of electrons, e.g. those which undergo hard bremsstrahlung at very small radius, may end up reconstructed as photons. The background from a resonant Z boson with an electron mis-identified as a photon comes primarily from Standard Model diboson processes. The dominant process is $WZ \to e\nu\ell\ell$, although there are smaller subleading processes such as $ZZ \to 4\ell$ in which one electron is out of the detector acceptance or mis-reconstructed.

The $e \to \gamma$ mis-identification rate is estimated by measuring the rate of Z boson decays in the reconstructed eγ and ee final states. The mis-identification rate is measured both in data ($\xi_{data}^{e\to\gamma}$) and MC simulation ($\xi_{MC}^{e\to\gamma}$) in bins of p_{T} and η. The dependence of the mis-identification rate as a function of $\langle\mu\rangle$, $E_{\text{T}}^{\text{miss}}$ and $m_{ee,e\gamma}$ window size is accounted for as additional systematic uncertainties. The $e \to \gamma$ mis-identification rate is approximately 1–2.5% in the barrel region of the detector. It increases to 2.5–5.5% in the endcap region because of the larger amount of material in front of the electromagnetic calorimeter.

A control region is defined in the same way as the signal region except that instead of requiring a signal photon, a *medium* electron is required with the same signal region kinematic topology selections. The $E_{\text{T}}^{\text{miss}}$ distribution in this control region is shown in Figure 2(a) and the MC simulation predicts that 93% of the events originate from the WZ process. Figure 2(b) shows the expected background from $e \to \gamma$ in the signal region as modeled by the MC simulation, the data in the control region scaled by $\xi_{data}^{e\to\gamma}$(open triangles), and the MC simulation in the control region scaled by $\xi_{MC}^{e\to\gamma}$ (closed squares).

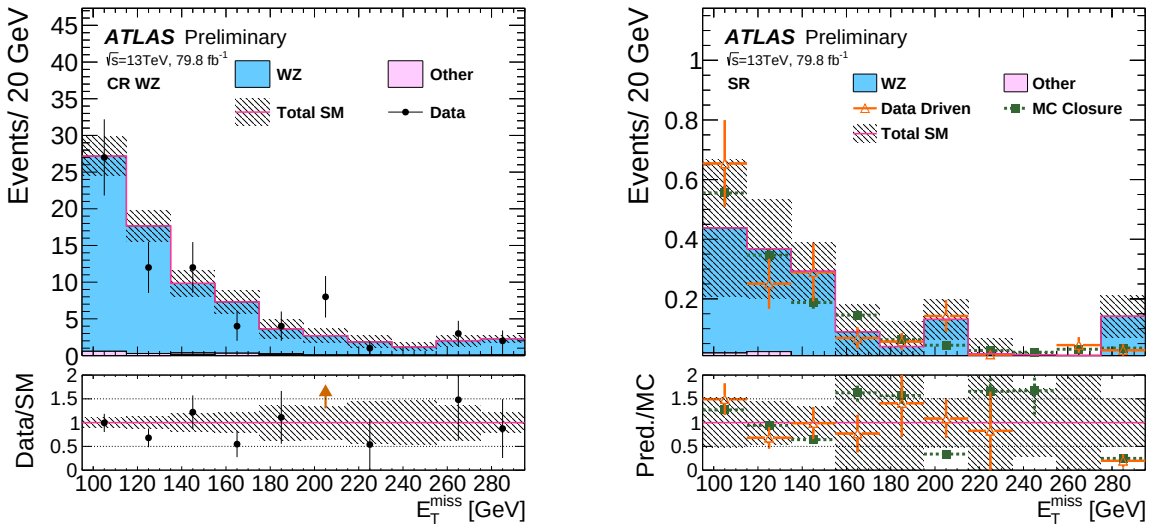

(a) $E_{\mathrm{T}}^{\mathrm{miss}}$ in the WZ control region

(b) $E_{\mathrm{T}}^{\mathrm{miss}}$ in the signal region

Figure 2: Distribution of $E_{\mathrm{T}}^{\mathrm{miss}}$ in (a) the WZ control region and (b) signal region for the $e \to \gamma$ background. Both regions are rich in WZ events. The other backgrounds include Z + jets, $t\bar{t}$, and diboson processes. In (b) the MC simulation is compared with the data-driven prediction (open triangles) and an MC closure test (closed squares). In both cases the uncertainty bands display the statistical error only.

4.2 Backgrounds from SM $Z\gamma$

Ideally, SM $Z\gamma$ events with no associated jets coming from the hard scatter should have no $E_{\mathrm{T}}^{\mathrm{miss}}$ as the momentum of the γ and Z boson should balance perfectly. Due to detector resolution, pileup of the underlying event and soft jets from multiple vertices, as well as heavy flavor quark decays in jets with $20 < p_{\mathrm{T}} < 30$ GeV, $E_{\mathrm{T}}^{\mathrm{miss}}$ is introduced into the event. Cutting higher on $E_{\mathrm{T}}^{\mathrm{miss}}$ is an effective strategy to reduce this background, although due to the kinematics of the Higgs boson decay, cutting very hard on $E_{\mathrm{T}}^{\mathrm{miss}}$ greatly reduces the signal acceptance, especially in the $h \to \tilde{\chi}_1^0\tilde{\chi}_1^0 \to \gamma\tilde{G}\gamma\tilde{G}$ decay channel.

A sample enriched with $Z\gamma$ events (CR $Z\gamma$) is defined at lower $E_{\mathrm{T}}^{\mathrm{miss}}$, requiring no cut on $\Delta\phi_{\ell\ell,\gamma E_{\mathrm{T}}^{\mathrm{miss}}}$, and a slightly looser cut on $\Delta\phi(\ell,\ell)$ in order to increase the number of events. This control region has 1203 events and is used to constrain the normalization of the $Z\gamma$ Monte Carlo. The shape and normalization of different variables are validated at intermediate $E_{\mathrm{T}}^{\mathrm{miss}}$ ($Z\gamma$ validation region). Figure 3 shows the $E_{\mathrm{T}}^{\mathrm{miss}}$ and $\mathrm{Bal}_{p_{\mathrm{T}}}$ distributions in this $Z\gamma$ validation region. Good data–MC agreement of different kinematic variables is observed in the $Z\gamma$ validation region.

4.3 Backgrounds with a jet faking a photon, mostly coming from Z +jets

The background arising from jets mis-identified as a photon comes primarily from Z +jets events and to a lesser extent, diboson/$t\bar{t}$ events with jets. The j $\to \gamma$ mis-identification rate is measured in a sample collected with an un-prescaled trigger requiring two photons; the first (second) highest-E_{T} photon is required to have $E_{\mathrm{T}} > 35$ (25) GeV, and both are required to pass identification criteria. Events are selected requiring one *tight* photon and one *loose* photon. The loose photons are then classified using

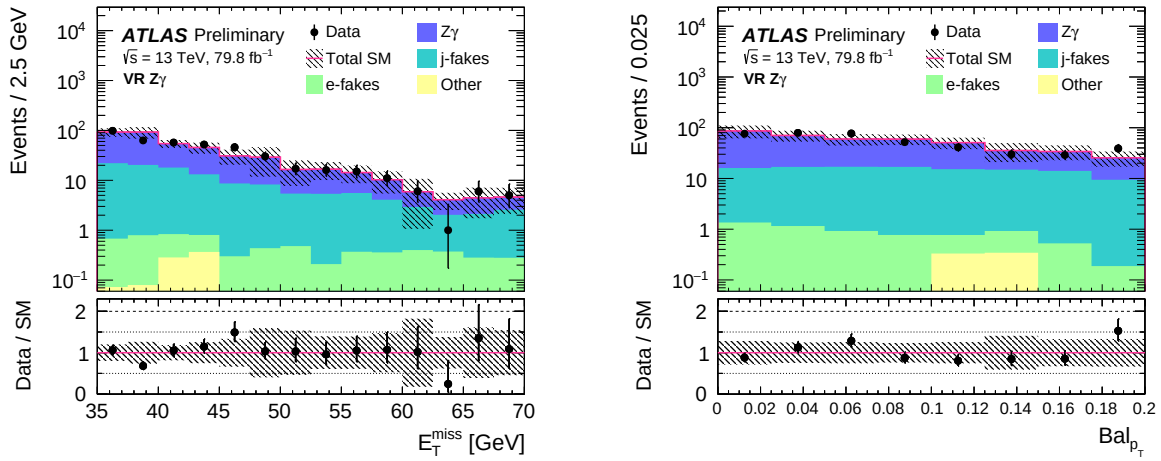

(a) $E_{\mathrm{T}}^{\mathrm{miss}}$ (b) $\mathrm{Bal}_{p_{\mathrm{T}}}$

Figure 3: Distributions of (a) $E_{\mathrm{T}}^{\mathrm{miss}}$ and (b) $\mathrm{Bal}_{p_{\mathrm{T}}}$ in the $Z\gamma$ validation region. The 'other' backgrounds come from $t\bar{t}\gamma$ and $V\gamma\gamma$ sources. The uncertainty bands plotted include all statistical and systematic uncertainties.

further identification requirements into two categories: *tight* and *loose-but-not-tight* ("pseudo"). This pseudo-photon is required to fail *tight* identification by failing at least one of the four electromagnetic calorimeter "narrow strip variable" criteria which are known to have small correlations with isolation [50]. A photon fake factor ($\kappa_{\mathrm{tight}}^{\mathrm{j}\to\gamma}$), defined as the number of *tight* photons divided by the number of pseudo-photons, is measured in a non-isolated region of $8 < E_{\mathrm{T}}^{0.4} - 0.22 \times p_{\mathrm{T}}^{\gamma} < 27\,\mathrm{GeV}$. This factor is measured to be 0.4–0.7 in the barrel region and 0.4–0.95 in the endcap region of the detector, depending on the p_{T} of the photon.

Additionally, the ratio of isolated pseudo-photons to all pseudo-photons is measured to be 0.17 in a looser version of the $Z\gamma$ control region, defined by removing the $\Delta\phi(\ell,\ell) < 2.0$ requirement. This ratio is seen to be constant as a function of different analysis variables in all regions of interest. All pseudo-photons are selected and then scaled by $\kappa_{\mathrm{tight}}^{\mathrm{j}\to\gamma} \times 0.17$. Figure 4 shows the $\mathrm{j} \to \gamma$ contribution in the $Z\gamma$ validation region (see section 4.2) where the estimate using isolated pseudo-photons is shown in open square markers, and the estimate using all (scaled) pseudo-photons is shown in closed triangle markers. The statistical uncertainty is greatly reduced for the second method, while the shape prediction is still accurate. The prediction of the $\mathrm{j} \to \gamma$ background in the signal region is estimated by selecting events with at least one pseudo-photon, instead of at least one signal photon, passing all signal region kinematic requirements and then scaling by $\kappa_{\mathrm{tight}}^{\mathrm{j}\to\gamma} \times 0.17$.

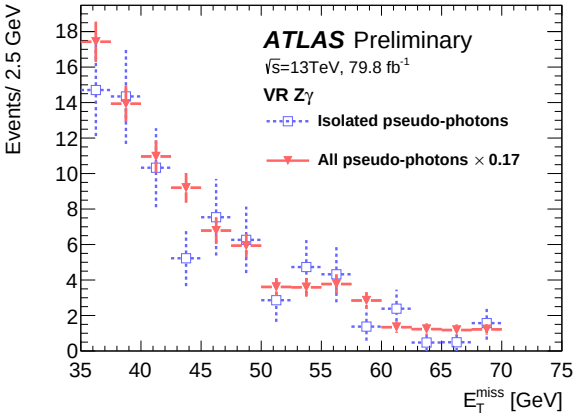

Figure 4: Distribution of $E_{\mathrm{T}}^{\mathrm{miss}}$ in the $Z\gamma$ validation region for the j $\rightarrow \gamma$ background using all (scaled) pseudo-photons (closed triangles) and using only isolated pseudo-photons (open squares). Only the statistical uncertainty of the prediction is shown.

5 Uncertainties

The signal and background predictions are affected by uncertainties from experimental sources, such as those on data-driven background estimation techniques, and uncertainties from the theoretical modeling of the simulated samples. A summary of the largest uncertainties on the background prediction in the signal region is shown in Table 3, where those less than 1.0% are excluded.

The largest uncertainties are from the data-driven background estimations and control region sample sizes. For the $e \rightarrow \gamma$ background, uncertainties are assigned to account for differences in the event topology and kinematic distributions between the region used to measure the fake rate and the signal region. These include the dependence of the fake rate as a function of $E_{\mathrm{T}}^{\mathrm{miss}}$, $\langle\mu\rangle$ and the size of the Z mass window used. The systematic uncertainties in the j $\rightarrow \gamma$ background come from the number of events in the region used to measure the fake rates, the correlation in control regions used for the fake factor measurement, and the pseudo-photon scaling factor.

The largest uncertainties on the simulated background and signal samples arise from $E_{\mathrm{T}}^{\mathrm{miss}}$ soft-term resolution modeling and uncertainty on the jet energy resolution. Also considered are uncertainties on the photon and lepton energy scale, energy resolution, identification efficiency, and isolation efficiency. Additionally, uncertainties on the lepton trigger efficiency and reconstruction efficiency are included. The uncertainty in the combined 2015–2017 integrated luminosity measurement used to normalize the simulated samples is 2.0%. It is derived, following a methodology similar to that detailed in Ref. [60], from calibrations of the luminosity scale using x–y beam-separation scans performed in August 2015, May 2016 and July 2017 (the results for 2017 are still preliminary). Finally, an uncertainty is assigned to the pileup re-weighting procedure that matches the $\langle\mu\rangle$ distribution in the simulated samples to that observed in data.

Cross-section theory uncertainties for $Z\gamma$, $t\bar{t}\gamma$, and $V\gamma\gamma$ production are considered, but change the total estimated background by less than 1% since the signal region background predictions come predominantly from data-driven sources. Cross-section theory uncertainties for the signal Zh production are also considered.

Total background expectation	2.1
Total systematic uncertainty	±0.5 [22%]
Uncertainty component	
CR WZ and jet fake sample size	±0.3 [15%]
Stat. error of $\kappa_{\text{tight}}^{\text{j}\to\gamma}$	±0.3 [12%]
$E_{\text{T}}^{\text{miss}}$ dependence of $\xi_{data}^{e\to\gamma}$	±0.1 [7%]
Jet energy resolution	±0.1 [6%]
$\xi_{MC}^{e\to\gamma}$ closure	±0.1 [5%]
$E_{\text{T}}^{\text{miss}}$ soft-term resolution	±0.1 [5%]
CR correlation $\kappa_{\text{tight}}^{\text{j}\to\gamma}$	±<0.1 [3%]
Pseudo photon scaling $\kappa_{\text{tight}}^{\text{j}\to\gamma}$	±<0.1 [2%]
Window dependence of $\xi_{data}^{e\to\gamma}$	±<0.1 [2%]
Photon/lepton energy scale	±<0.1 [2%]
Photon isolation	±<0.1 [2%]
$\langle\mu\rangle$ dependence of $\xi_{data}^{e\to\gamma}$	±<0.1 [1%]
Jet energy scale	±<0.1 [1%]

Table 3: Breakdown of the systematic uncertainties (greater than 1.0%) on background estimates in the signal region. The percent column show the size of the uncertainty relative to the total expected number of background events. Twelve uncertainty components are below the 1% threshold and not included in this table.

6 Results

The HistFitter framework [61] is used for the statistical interpretation of the results. This framework simultaneously fits the signal and control regions, constructing a likelihood defined as the product of Poisson probability density functions (PDFs) [62]. The Poisson PDFs describe the number of observed events in each region, with systematic uncertainties treated as Gaussian nuisance parameters.

To determine the SM background predictions independently of the signal region, a background-only fit is done, using the control region to constrain the fit parameters via likelihood maximization. This fit assumes no signal events are present in the control region. The normalization of the $Z\gamma$ Monte Carlo, $\mu_{Z\gamma}$ is 1.04 ± 0.13 where the uncertainty is the combination of statistical and systematic components.

Observed events	3
Expected background events	2.1 ± 0.5
Expected signal events $m_{NLSP}, m_{LSP} = 80, 0$ GeV	8.1
$e \to \gamma$ fakes	1.5 ± 0.3
$\text{j} \to \gamma$ fakes	0.6 ± 0.3
SM $Z\gamma$	$0.03^{+0.15}_{-0.03}$
Other	$0.00^{+0.01}_{-0.00}$

Table 4: Table of the expected and observed number of events in the signal region. For comparison, the yield from an $m_{\tilde{\chi}_1^0}, m_{\tilde{G}} = 80, 0$ GeV signal is shown.

Three events are observed in the signal region above the expected 2.1 background events. The probability of the three observed events to be consistent with the expected background of 2.1 ± 0.5 is $p_0 = 0.32$ (< 1

σ). These results are summarized in Table 4, as well as illustrated in Figure 5, with the expected number of background events broken down into its various components. No significant excess above the Standard Model expectation is observed.

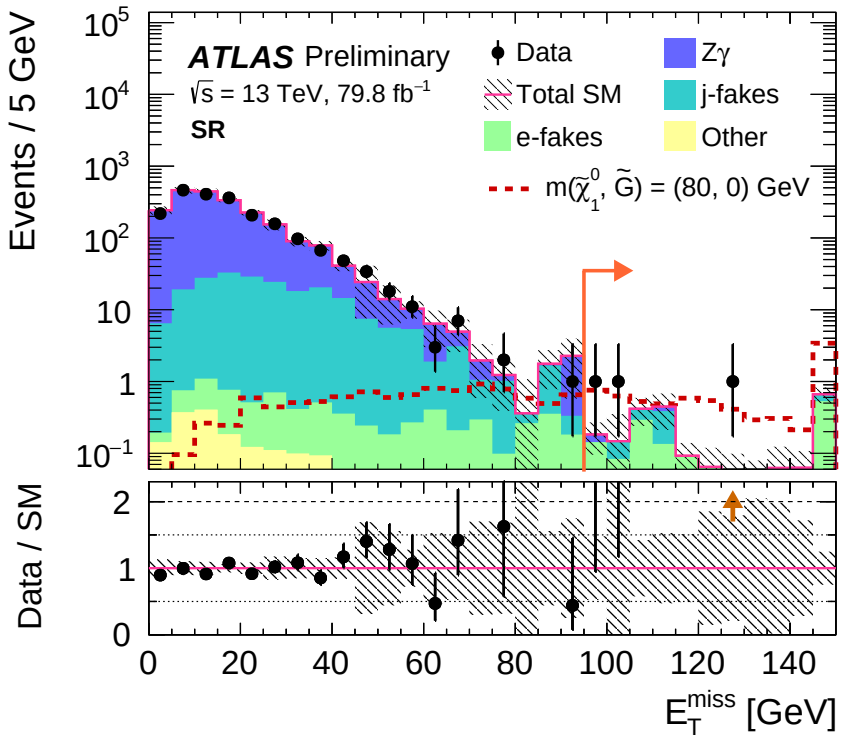

Figure 5: Distribution of $E_{\mathrm{T}}^{\mathrm{miss}}$ in the signal region. The orange arrow indicates the signal region. The contribution from $Z\gamma$ and other ($t\bar{t}\gamma$, $V\gamma\gamma$) sources is expected to be 0.03 events in the signal region. The red dashed line overlays the predictions from a signal benchmark with $m_{\tilde{\chi}_1^0}, m_{\tilde{G}} = 80, 0\,\mathrm{GeV}$. The uncertainty bands plotted include all statistical and systematic uncertainties.

The observed and expected number of events in the signal region is used to set upper limits on model-independent properties of BSM processes and the branching fraction of the $h \to \tilde{\chi}_1^0\tilde{\chi}_1^0 \to \gamma\tilde{G}\gamma\tilde{G}$ and $h \to \tilde{\chi}_1^0\tilde{G} \to \gamma\tilde{G}\tilde{G}$ processes assuming a SM Zh production. Following the $\mathrm{CL_s}$ method [63], a one-side profile likelihood ratio test statistic is used to set upper limits at the 95% CL. The test statistics estimator is derived with pseudo-experiments. Table 5 shows the model-independent limits in the signal region. The upper limit on the visible cross section $\langle\epsilon\sigma\rangle_{\mathrm{obs}}^{95}$ is obtained by dividing the number of signal events S_{obs}^{95} by the integrated luminosity of $79.8\,\mathrm{fb}^{-1}$. The expected number of signal events S_{exp}^{95} and p-value, quantifying the probability for the background hypothesis to fluctuate at or above the observed number of events, are also given. The 95% CL upper limits on the model-dependent $h \to \tilde{\chi}_1^0\tilde{\chi}_1^0 \to \gamma\tilde{G}\gamma\tilde{G}$ ($h \to \tilde{\chi}_1^0\tilde{G} \to \gamma\tilde{G}\tilde{G}$) branching fraction can be seen in Figure 6 (7). For the $h \to \tilde{\chi}_1^0\tilde{\chi}_1^0 \to \gamma\tilde{G}\gamma\tilde{G}$ signature, $\mathrm{BF}(h \to \tilde{\chi}_1^0\tilde{G} \to \gamma\tilde{G}\tilde{G})$ is assumed to be zero and vice versa. The observed upper limits of the branching fraction of Higgs boson decays to one or two photons plus $E_{\mathrm{T}}^{\mathrm{miss}}$ range from 5–18% depending on NLSP and LSP masses.

$\langle\epsilon\sigma\rangle^{95}_{\rm obs}$[fb]	$S^{95}_{\rm obs}$	$S^{95}_{\rm exp}$	$p(s=0)$
0.06	5.1	$4.5^{+1.9}_{-1.0}$	0.32

Table 5: Table of the model-independent 95% CL upper limits on the visible cross section $\langle\epsilon\sigma\rangle^{95}_{\rm obs}$ and on the number of signal events S^{95}_{obs}. The third column ($S^{95}_{\rm exp}$) shows the 95% CL upper limit on the number of signal events, given the expected number (and ±1 σ excursions on the expectation) of background events. The last column indicates the background only hypothesis p-value $p(s=0)$.

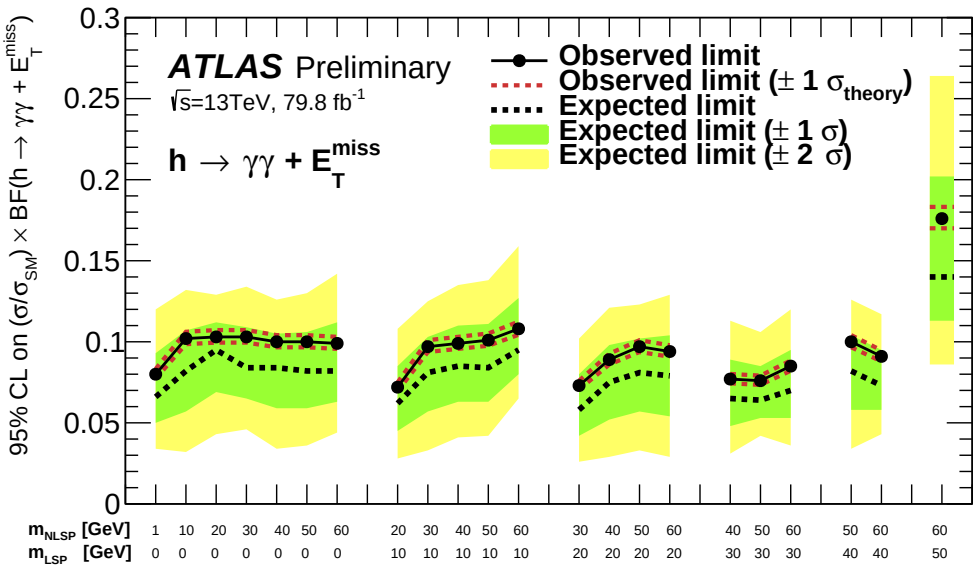

Figure 6: 95% CL observed and expected limits of $(\sigma/\sigma_{SM}) \times \mathrm{BF}(h \to \gamma\gamma + E_{\rm T}^{\rm miss})$ for various NLSP and LSP masses. The inner and outer bands show the ±1 σ and ±2 σ excursions of the expected limits respectively. These limits are for the case $0 < m_{\rm NLSP} < m_h/2$ and the Higgs boson is assumed to decay to a $\gamma\gamma + E_{\rm T}^{\rm miss}$ final state.

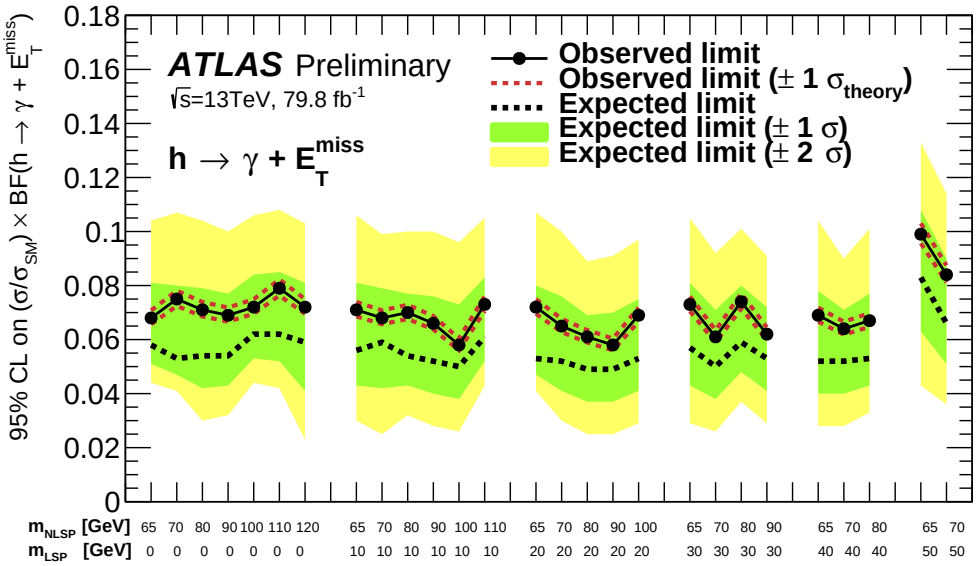

Figure 7: 95% CL observed and expected limits of $(\sigma/\sigma_{SM}) \times \mathrm{BF}(h \to \gamma + E_{\mathrm{T}}^{\mathrm{miss}})$ for various NLSP and LSP masses. The inner and outer bands show the $\pm 1\ \sigma$ and $\pm 2\ \sigma$ excursions of the expected limits respectively. These limits are for the case $m_h/2 < m_{\mathrm{NLSP}} < m_h$ and the Higgs boson is assumed to decay to a $\gamma + E_{\mathrm{T}}^{\mathrm{miss}}$ final state.

7 Conclusion

A search for $h \to \tilde{\chi}_1^0\tilde{\chi}_1^0 \to \gamma\tilde{G}\gamma\tilde{G}$ and $h \to \tilde{\chi}_1^0\tilde{G} \to \gamma\tilde{G}\tilde{G}$ processes is performed, selecting events with two opposite-sign leptons, at least one photon and missing transverse momentum using an integrated luminosity of $79.8\,\mathrm{fb}^{-1}$ of proton–proton collisions collected at $\sqrt{s} = 13\,\mathrm{TeV}$ with the ATLAS detector. Three events are observed in the signal region, where 2.1 events are expected. Since no significant excess is observed with respect to the Standard Model prediction, upper limits at 95% CL of less than 11% (18%) on the cross-section times branching fraction of each process are observed for massless gravitinos (massive neutralinos).

References

[1] ATLAS Collaboration, *Observation of a new particle in the search for the Standard Model Higgs boson with the ATLAS detector at the LHC*, Phys. Lett. B **716** (2012) 1, arXiv: 1207.7214 [hep-ex].

[2] CMS Collaboration, *Observation of a new boson at a mass of 125 GeV with the CMS experiment at the LHC*, Phys. Lett. B **716** (2012) 30, arXiv: 1207.7235 [hep-ex].

[3] L. Evans and P. Bryant, *LHC Machine*, JINST **3** (2008).

[4] ATLAS and CMS Collaborations,
Measurements of the Higgs boson production and decay rates and constraints on its couplings from a combined ATLAS and CMS analysis of the LHC pp collision data at $\sqrt{s}$ = 7 and 8 TeV,
JHEP **08** (2016) 045, arXiv: 1606.02266 [hep-ex].

[5] CMS Collaboration, *Combined measurements of the Higgs boson's couplings at $\sqrt{s}$ = 13 TeV*,
CMS-PAS-HIG-17-031, 2018, URL: https://cds.cern.ch/record/2308127.

[6] D. Curtin et al., *Exotic decays of the 125 GeV Higgs boson*, Phys. Rev. D **90** (2014) 075004,
arXiv: 1312.4992 [hep-ph].

[7] Yu. A. Golfand and E. P. Likhtman,
Extension of the Algebra of Poincare Group Generators and Violation of p Invariance,
JETP Lett. **13** (1971) 323, [Pisma Zh. Eksp. Teor. Fiz. **13**, 452(1971)].

[8] D. Volkov and V. Akulov, *Is the Neutrino a Goldstone Particle?*, Phys. Lett. B **46** (1973) 109.

[9] J. Wess and B. Zumino, *Supergauge Transformations in Four Dimensions*,
Nucl. Phys. B **70** (1974) 39.

[10] J. Wess and B. Zumino, *Supergauge invariant extension of quantum electrodynamics*,
Nucl. Phys. B **78** (1974) 1.

[11] S. Ferrara and B. Zumino, *Supergauge invariant Yang-Mills theories*,
Nucl. Phys. B **79** (1974) 413.

[12] A. Salam and J. Strathdee, *Super-symmetry and non-Abelian gauges*, Phys. Lett. B **51** (1974) 353.

[13] M. Dine and W. Fischler, *A phenomenological model of particle physics based on supersymmetry*,
Phys. Lett. B **110** (1982) 227.

[14] L. Alvarez-Gaumé, M. Claudson and M. B. Wise, *Low-energy supersymmetry*,
Nucl. Phys. B **207** (1982) 96.

[15] C. R. Nappi and B. A. Ovrut, *Supersymmetric extension of the SU(3)×SU(2)×U(1) model*,
Phys. Lett. B **113** (1982) 175.

[16] M. Dine and A. E. Nelson, *Dynamical supersymmetry breaking at low energies*,
Phys. Rev. D **48** (1993) 1277, arXiv: hep-ph/9303230 [hep-ph].

[17] M. Dine, A. E. Nelson, Y. Nir and Y. Shirman,
New tools for low energy dynamical supersymmetry breaking, Phys. Rev. D **53** (1996) 2658,
arXiv: hep-ph/9507378 [hep-ph].

[18] N. Craig, D. Green and A. Katz,
(De)constructing a natural and flavorful supersymmetric Standard Model, JHEP **07** (2011) 45,
arXiv: 1103.3708 [hep-ph].

[19] R. Auzzi, A. Giveon and S. B. Gudnason,
Flavor of quiver-like realizations of effective supersymmetry, JHEP **02** (2012) 69,
arXiv: 1112.6261 [hep-ph].

[20] C. Csáki, L. Randall and J. Terning, *Light stops from Seiberg duality*,
Phys. Rev. D **86** (2012) 075009, arXiv: 1201.1293 [hep-ph].

[21] N. Craig, S. Dimopoulos and T. Gherghetta, *Split families unified*, JHEP **04** (2012) 116,
arXiv: 1203.0572 [hep-ph].

[22] G. Larsen, Y. Nomura and H. L. L. Roberts, *Supersymmetry with light stops*, JHEP **06** (2012) 32, arXiv: 1202.6339 [hep-ph].

[23] C. Petersson, A. Romagnoni and R. Torre, *Higgs Decay with Monophoton + MET Signature from Low Scale Supersymmetry Breaking*, JHEP **10** (2012) 016, arXiv: 1203.4563 [hep-ph].

[24] J. Ellis, J. F. Gunion, H. E. Haber, L. Roszkowski and F. Zwirner, *Higgs bosons in a nonminimal supersymmetric model*, Phys. Rev. D **39** (1989) 844.

[25] J. Huang, T. Liu, L.-T. Wang and F. Yu, *Supersymmetric Exotic Decays of the 125 GeV Higgs Boson*, Phys. Rev. Lett. **112** (2014) 221803, arXiv: 1309.6633 [hep-ph].

[26] J. D. Mason, D. E. Morrissey and D. Poland, *Higgs Boson Decays to Neutralinos in Low-Scale Gauge Mediation*, Phys. Rev. D **80** (2009) 115015, arXiv: 0909.3523 [hep-ph].

[27] ATLAS Collaboration, *Search for exotic Higgs-boson decays in events with at least one photon, missing transverse momentum, and two forward jets produced in $\sqrt{s}$ = 8 TeV pp collisions with the ATLAS detector*, ATLAS-CONF-2015-001, 2015, URL: https://cds.cern.ch/record/1988425.

[28] CMS Collaboration, *Search for exotic decays of a Higgs boson into undetectable particles and one or more photons*, Phys. Lett. B **753** (2016) 363, arXiv: 1507.00359 [hep-ex].

[29] ATLAS Collaboration, *The ATLAS Experiment at the CERN Large Hadron Collider*, JINST **3** (2008) S08003.

[30] ATLAS Collaboration, *Performance of the ATLAS Trigger System in 2015*, Eur. Phys. J. C **77** (2017) 317, arXiv: 1611.09661 [hep-ex].

[31] T. Gleisberg et al., *Event generation with SHERPA 1.1*, JHEP **02** (2009) 007, arXiv: 0811.4622 [hep-ph].

[32] S. Höche, F. Krauss, M. Schönherr and F. Siegert, *QCD matrix elements + parton showers: The NLO case*, JHEP **04** (2013) 027, arXiv: 1207.5030 [hep-ph].

[33] R. D. Ball et al., *Parton distributions for the LHC Run II*, JHEP **04** (2015) 040, arXiv: 1410.8849 [hep-ph].

[34] S. Schumann and F. Krauss, *A Parton shower algorithm based on Catani-Seymour dipole factorisation*, JHEP **03** (2008) 038, arXiv: 0709.1027 [hep-ph].

[35] J. Alwall et al., *The automated computation of tree-level and next-to-leading order differential cross sections, and their matching to parton shower simulations*, JHEP **07** (2014) 079, arXiv: 1405.0301 [hep-ph].

[36] R. D. Ball et al., *Parton distributions with LHC data*, Nucl. Phys. B **867** (2013) 244, arXiv: 1207.1303 [hep-ph].

[37] ATLAS Collaboration, *ATLAS Pythia 8 tunes to 7 TeV data*, ATL-PHYS-PUB-2014-021, 2014.

[38] T. Sjöstrand et al., *An Introduction to PYTHIA 8.2*, Comput. Phys. Commun. **191** (2015) 159, arXiv: 1410.3012 [hep-ph].

[39] T. Sjöstrand, S. Mrenna and P. Z. Skands, *PYTHIA 6.4 Physics and Manual*, JHEP **05** (2006) 026, arXiv: hep-ph/0603175 [hep-ph].

[40] T. Sjöstrand, S. Mrenna and P. Z. Skands, *A Brief Introduction to PYTHIA 8.1*, Comput. Phys. Commun. **178** (2008) 852, arXiv: 0710.3820 [hep-ph].

[41] S. Agostinelli et al., *GEANT4: A Simulation toolkit*, Nucl. Instrum. Meth. A **506** (2003) 250.

[42] ATLAS Collaboration, *The ATLAS Simulation Infrastructure*, Eur. Phys. J. C **70** (2010) 823, arXiv: 1005.4568 [physics.ins-det].

[43] J. Alwall, P. C. Schuster and N. Toro, *Simplified models for a first characterization of new physics at the LHC*, Phys. Rev. D **79** (2009) 075020, arXiv: 0810.3921 [hep-ph].

[44] D. Alves et al., *Simplified models for LHC new physics searches*, Nucl. Phys. G **39** (2012) 105005, arXiv: 1105.2838 [hep-ph].

[45] ATLAS Collaboration, *The simulation principle and performance of the ATLAS fast calorimeter simulation FastCaloSim*, ATL-PHYS-PUB-2010-013, 2010, URL: https://cds.cern.ch/record/1300517.

[46] D. de Florian et al., *Handbook of LHC Higgs Cross Sections: 4. Deciphering the Nature of the Higgs Sector*, (2016), arXiv: 1610.07922 [hep-ph].

[47] ATLAS Collaboration, *Summary of ATLAS Pythia 8 tunes*, ATL-PHYS-PUB-2012-003, 2012, URL: https://cds.cern.ch/record/1474107.

[48] ATLAS Collaboration, *Prospects for a search for direct pair production of top squarks in scenarios with compressed mass spectra at the high luminosity LHC with the ATLAS Detector*, ATL-PHYS-PUB-2016-022, 2016, URL: https://cds.cern.ch/record/2220904.

[49] ATLAS Collaboration, *Electron efficiency measurements with the ATLAS detector using 2012 LHC proton–proton collision data*, Eur. Phys. J. C **77** (2017) 195, arXiv: 1612.01456 [hep-ex].

[50] ATLAS Collaboration, *Photon identification in 2015 ATLAS data*, ATL-PHYS-PUB-2016-014, 2016, URL: https://cds.cern.ch/record/2203125.

[51] ATLAS Collaboration, *Electron efficiency measurements with the ATLAS detector using the 2015 LHC proton–proton collision data*, ATLAS-CONF-2016-024, 2016, URL: https://cds.cern.ch/record/2157687.

[52] ATLAS Collaboration, *Muon reconstruction performance in early* $\sqrt{s} = 13$ *TeV data*, ATL-PHYS-PUB-2015-037, 2015, URL: https://cds.cern.ch/record/2047831.

[53] M. Cacciari, G. P. Salam and G. Soyez, *The Anti-k(t) jet clustering algorithm*, JHEP **04** (2008) 063, arXiv: 0802.1189 [hep-ph].

[54] ATLAS Collaboration, *Jet energy scale measurements and their systematic uncertainties in proton–proton collisions at* $\sqrt{s} = 13$ *TeV with the ATLAS detector*, Phys. Rev. D **96** (2017) 072002, arXiv: 1703.09665 [hep-ex].

[55] ATLAS Collaboration, *Selection of jets produced in* 13 *TeV proton–proton collisions with the ATLAS detector*, ATLAS-CONF-2015-029, 2015, URL: https://cds.cern.ch/record/2037702.

[56] ATLAS Collaboration, *Performance of pile-up mitigation techniques for jets in pp collisions at $\sqrt{s}$ = 8 TeV using the ATLAS detector*, Eur. Phys. J. C **76** (2016) 581, arXiv: 1510.03823 [hep-ex].

[57] ATLAS Collaboration, *Performance of missing transverse momentum reconstruction with the ATLAS detector using proton-proton collisions at $\sqrt{s}$ = 13 TeV*, (2018), arXiv: 1802.08168 [hep-ex].

[58] C. Patrignani et al., *Review of Particle Physics*, Chin. Phys. **C40** (2016) 100001.

[59] ATLAS Collaboration, *Searches for the $Z\gamma$ decay mode of the Higgs boson and for new high-mass resonances in pp collisions at $\sqrt{s}$ = 13 TeV with the ATLAS detector*, JHEP **10** (2017) 112, arXiv: 1708.00212 [hep-ex].

[60] ATLAS Collaboration, *Luminosity determination in pp collisions at $\sqrt{s}$ = 8 TeV using the ATLAS detector at the LHC*, Eur. Phys. J. C **76** (2016) 653, arXiv: 1608.03953 [hep-ex].

[61] M. Baak et al., *HistFitter software framework for statistical data analysis*, Eur. Phys. J. C **75** (2015) 153, arXiv: 1410.1280 [hep-ex].

[62] G. Cowan, K. Cranmer, E. Gross and O. Vitells, *Asymptotic formulae for likelihood-based tests of new physics*, Eur. Phys. J. C **71** (2011) 1554, arXiv: 1007.1727 [physics.data-an].

[63] A. L. Read, *Presentation of search results: the CL s technique*, Nucl. Phys. G **28** (2002) 2693.

Appendix

The 95% CL upper limits on the $h \to \tilde{\chi}_1^0\tilde{\chi}_1^0 \to \gamma\tilde{G}\gamma\tilde{G}$ ($h \to \tilde{\chi}_1^0\tilde{G} \to \gamma\tilde{G}\tilde{G}$) branching fraction is shown in Table 6 (7).

Signal channel	BF($h \to \gamma\gamma + E_{\mathrm{T}}^{\mathrm{miss}}$)$^{95}_{\mathrm{obs}}$	BF($h \to \gamma\gamma + E_{\mathrm{T}}^{\mathrm{miss}}$)$^{95}_{\mathrm{exp}}$
$m_{NLSP}, m_{LSP} = 1, 0$ GeV	0.080	$0.066^{+0.027}_{-0.016}$
$m_{NLSP}, m_{LSP} = 10, 0$ GeV	0.102	$0.081^{+0.025}_{-0.025}$
$m_{NLSP}, m_{LSP} = 11, 10$ GeV	0.359	$0.292^{+0.175}_{-0.103}$
$m_{NLSP}, m_{LSP} = 20, 0$ GeV	0.103	$0.095^{+0.017}_{-0.026}$
$m_{NLSP}, m_{LSP} = 20, 10$ GeV	0.072	$0.062^{+0.023}_{-0.017}$
$m_{NLSP}, m_{LSP} = 21, 20$ GeV	3.618	$2.939^{+1.842}_{-1.047}$
$m_{NLSP}, m_{LSP} = 30, 0$ GeV	0.103	$0.084^{+0.025}_{-0.019}$
$m_{NLSP}, m_{LSP} = 30, 10$ GeV	0.097	$0.081^{+0.022}_{-0.024}$
$m_{NLSP}, m_{LSP} = 30, 20$ GeV	0.073	$0.058^{+0.022}_{-0.016}$
$m_{NLSP}, m_{LSP} = 31, 30$ GeV	5.744	$4.426^{+1.574}_{-2.102}$
$m_{NLSP}, m_{LSP} = 40, 0$ GeV	0.100	$0.084^{+0.021}_{-0.025}$
$m_{NLSP}, m_{LSP} = 40, 10$ GeV	0.099	$0.085^{+0.025}_{-0.022}$
$m_{NLSP}, m_{LSP} = 40, 20$ GeV	0.089	$0.075^{+0.023}_{-0.023}$
$m_{NLSP}, m_{LSP} = 40, 30$ GeV	0.077	$0.065^{+0.024}_{-0.017}$
$m_{NLSP}, m_{LSP} = 41, 40$ GeV	17.203	$12.986^{+7.014}_{-7.039}$
$m_{NLSP}, m_{LSP} = 50, 0$ GeV	0.100	$0.082^{+0.024}_{-0.023}$
$m_{NLSP}, m_{LSP} = 50, 10$ GeV	0.101	$0.084^{+0.027}_{-0.021}$
$m_{NLSP}, m_{LSP} = 50, 20$ GeV	0.097	$0.081^{+0.021}_{-0.024}$
$m_{NLSP}, m_{LSP} = 50, 30$ GeV	0.076	$0.064^{+0.021}_{-0.011}$
$m_{NLSP}, m_{LSP} = 50, 40$ GeV	0.100	$0.082^{+0.022}_{-0.024}$
$m_{NLSP}, m_{LSP} = 51, 50$ GeV	4.430	$3.590^{+2.318}_{-1.294}$
$m_{NLSP}, m_{LSP} = 60, 0$ GeV	0.099	$0.082^{+0.030}_{-0.019}$
$m_{NLSP}, m_{LSP} = 60, 10$ GeV	0.108	$0.095^{+0.015}_{-0.032}$
$m_{NLSP}, m_{LSP} = 60, 20$ GeV	0.094	$0.079^{+0.025}_{-0.025}$
$m_{NLSP}, m_{LSP} = 60, 30$ GeV	0.085	$0.070^{+0.025}_{-0.017}$
$m_{NLSP}, m_{LSP} = 60, 40$ GeV	0.091	$0.073^{+0.022}_{-0.015}$
$m_{NLSP}, m_{LSP} = 60, 50$ GeV	0.176	$0.140^{+0.062}_{-0.027}$
$m_{NLSP}, m_{LSP} = 61, 60$ GeV	8.601	$6.948^{+4.730}_{-2.560}$

Table 6: 95% CL upper limits on the BF($h \to \gamma\gamma + E_{\mathrm{T}}^{\mathrm{miss}}$) assuming a SM Higgs boson production cross section. The second column (BF($h \to \gamma\gamma + E_{\mathrm{T}}^{\mathrm{miss}}$)$^{95}_{\mathrm{exp}}$) shows the 95% CL upper limit on the BF($h \to \gamma\gamma + E_{\mathrm{T}}^{\mathrm{miss}}$) given the expected number (and $\pm 1\sigma$ excursions on the expectation) of background events. These limits are for the case $0 < m_{\mathrm{NLSP}} < m_h/2$ and the Higgs boson is assumed to decay to a $\gamma\gamma + E_{\mathrm{T}}^{\mathrm{miss}}$ final state.

Signal channel	BF($h \to \gamma + E_{\mathrm{T}}^{\mathrm{miss}}$)$^{95}_{\mathrm{obs}}$	BF($h \to \gamma + E_{\mathrm{T}}^{\mathrm{miss}}$)$^{95}_{\mathrm{exp}}$
m_{NLSP}, m_{LSP} = 65, 0 GeV	0.068	$0.058^{+0.023}_{-0.007}$
m_{NLSP}, m_{LSP} = 65, 10 GeV	0.071	$0.056^{+0.025}_{-0.013}$
m_{NLSP}, m_{LSP} = 65, 20 GeV	0.072	$0.053^{+0.027}_{-0.006}$
m_{NLSP}, m_{LSP} = 65, 30 GeV	0.073	$0.057^{+0.024}_{-0.014}$
m_{NLSP}, m_{LSP} = 65, 40 GeV	0.069	$0.052^{+0.026}_{-0.012}$
m_{NLSP}, m_{LSP} = 65, 50 GeV	0.099	$0.083^{+0.025}_{-0.020}$
m_{NLSP}, m_{LSP} = 70, 0 GeV	0.075	$0.053^{+0.027}_{-0.006}$
m_{NLSP}, m_{LSP} = 70, 10 GeV	0.068	$0.059^{+0.020}_{-0.017}$
m_{NLSP}, m_{LSP} = 70, 20 GeV	0.065	$0.052^{+0.024}_{-0.011}$
m_{NLSP}, m_{LSP} = 70, 30 GeV	0.061	$0.050^{+0.021}_{-0.012}$
m_{NLSP}, m_{LSP} = 70, 40 GeV	0.064	$0.052^{+0.019}_{-0.012}$
m_{NLSP}, m_{LSP} = 70, 50 GeV	0.084	$0.066^{+0.024}_{-0.015}$
m_{NLSP}, m_{LSP} = 80, 0 GeV	0.071	$0.054^{+0.025}_{-0.012}$
m_{NLSP}, m_{LSP} = 80, 10 GeV	0.070	$0.054^{+0.023}_{-0.011}$
m_{NLSP}, m_{LSP} = 80, 20 GeV	0.061	$0.049^{+0.020}_{-0.012}$
m_{NLSP}, m_{LSP} = 80, 30 GeV	0.074	$0.059^{+0.021}_{-0.011}$
m_{NLSP}, m_{LSP} = 80, 40 GeV	0.067	$0.053^{+0.024}_{-0.010}$
m_{NLSP}, m_{LSP} = 90, 0 GeV	0.069	$0.054^{+0.023}_{-0.011}$
m_{NLSP}, m_{LSP} = 90, 10 GeV	0.066	$0.052^{+0.024}_{-0.012}$
m_{NLSP}, m_{LSP} = 90, 20 GeV	0.058	$0.049^{+0.021}_{-0.012}$
m_{NLSP}, m_{LSP} = 90, 30 GeV	0.062	$0.053^{+0.019}_{-0.012}$
m_{NLSP}, m_{LSP} = 100, 0 GeV	0.072	$0.062^{+0.022}_{-0.009}$
m_{NLSP}, m_{LSP} = 100, 10 GeV	0.058	$0.050^{+0.023}_{-0.012}$
m_{NLSP}, m_{LSP} = 100, 20 GeV	0.069	$0.053^{+0.022}_{-0.012}$
m_{NLSP}, m_{LSP} = 110, 0 GeV	0.079	$0.062^{+0.023}_{-0.010}$
m_{NLSP}, m_{LSP} = 110, 10 GeV	0.073	$0.061^{+0.022}_{-0.009}$
m_{NLSP}, m_{LSP} = 120, 0 GeV	0.072	$0.059^{+0.022}_{-0.018}$

Table 7: 95% CL upper limits on the BF($h \to \gamma + E_{\mathrm{T}}^{\mathrm{miss}}$) assuming a SM Higgs boson production cross section. The second column (BF($h \to \gamma + E_{\mathrm{T}}^{\mathrm{miss}}$)$^{95}_{\mathrm{exp}}$) shows the 95% CL upper limit on the BF($h \to \gamma + E_{\mathrm{T}}^{\mathrm{miss}}$) given the expected number (and $\pm 1\sigma$ excursions on the expectation) of background events. These limits are for the case $m_h/2 < m_{\mathrm{NLSP}} < m_h$ and the Higgs boson is assumed to decay to a $\gamma + E_{\mathrm{T}}^{\mathrm{miss}}$ final state.